

No Thick Atmosphere on the Terrestrial Exoplanet Gl 486b

MEGAN WEINER MANSFIELD,^{1,2,3} QIAO XUE,⁴ MICHAEL ZHANG,^{4,5} ALEXANDRA S. MAHAJAN,⁶ JEGUG IH,⁷ DANIEL KOLL,⁸
JACOB L. BEAN,⁴ BRANDON PARK COY,⁹ JASON D. EASTMAN,⁶ ELIZA M.-R. KEMPTON,⁷ AND EDWIN S. KITE⁹

¹*Steward Observatory, University of Arizona, Tucson, AZ, USA*

²*School of Earth and Space Exploration, Arizona State University, Tempe, AZ, USA*

³*NHFP Sagan Fellow*

⁴*Department of Astronomy & Astrophysics, University of Chicago, Chicago, IL, USA*

⁵*51 Pegasi b fellow*

⁶*Center for Astrophysics | Harvard & Smithsonian, 60 Garden St, Cambridge, MA, USA*

⁷*Department of Astronomy, University of Maryland, College Park, MD, USA*

⁸*Peking University, Beijing, People's Republic of China*

⁹*Department of Geophysical Sciences, University of Chicago, Chicago, IL, USA*

ABSTRACT

A primary science goal for *JWST* is to detect and characterize the atmospheres of terrestrial planets orbiting M dwarfs (M-Earths). The existence of atmospheres on M-Earths is highly uncertain because their host stars' extended history of high XUV irradiation may act to completely remove their atmospheres. We present two *JWST* secondary eclipse observations of the M-Earth Gl 486b (also known as GJ 486b) between 5 – 12 μm . We combined these observations with a precise analysis of the host star parameters to derive a planetary dayside temperature of $T_p = 865 \pm 14$ K. We compared this temperature to the maximum expected temperature for a zero albedo, zero heat redistribution bare rock and derived a temperature ratio of $\mathcal{R} = \frac{T_{p, \text{dayside}}}{T_{p, \text{max}}} = 0.97 \pm 0.01$. This value is consistent with an airless body with a slight non-zero albedo or a thin atmosphere with $< 1\%$ H₂O or < 1 ppm CO₂. However, it is inconsistent with an Earth- or Venus-like atmosphere, and the spectrum shows no clear emission or absorption features. Additionally, our observations are inconsistent with the water-rich atmospheric scenario allowed by previous transit observations and suggest the transmission spectrum was instead shaped by stellar contamination (Moran et al. 2023). Given the potential for atmospheric escape throughout the system's ≥ 6.6 -Gyr lifetime (Diamond-Lowe et al. 2024), we conclude that the observations are likely best explained by an airless planet. This result is the most precise measurement yet of terrestrial exoplanet thermal emission with *JWST*, which places a strong constraint on the position of the “Cosmic Shoreline” between airless bodies and those with atmospheres.

1. INTRODUCTION

A key goal of *JWST* is to identify and characterize atmospheres on terrestrial planets. In particular, *JWST* is the first facility capable of searching for atmospheres on a large sample of rocky planets orbiting M dwarfs (M-Earths). However, the ability of M-Earths to retain atmospheres over geologic timescales is highly uncertain. The high X-ray and ultraviolet flux (XUV) of young M dwarfs (e.g., Tian 2009; Davenport et al. 2012), and their high flare rates at older ages (Johnstone 2020) may strip terrestrial planets in close-in orbits of their atmospheres.

Studies of solar system bodies have suggested that atmospheric loss or retention is determined by a body's position relative to the “Cosmic Shoreline”, a dividing line which separates bodies at low bolometric or XUV fluxes which are able to retain atmospheres from the air-

less bodies at high bolometric/XUV flux, as a function of surface gravity (Zahnle & Catling 2017). Extending this theory to M-Earths a priori is complicated by several unknown factors, such as the variation in XUV flux among similar stars (West et al. 2008); and the effects of atomic line cooling (Nakayama et al. 2022), initial volatile inventory (Kite & Barnett 2020), and the timing of volatile delivery (Dorn & Heng 2018) or outgassing (Tian 2009) on the prevalence of atmospheres on M-Earths. Therefore, a first order goal of *JWST* exoplanet science is to precisely measure the presence or absence of atmospheres on M-Earths to observationally constrain the location of this “Cosmic Shoreline”.

Gl 486b, also known as GJ 486b, is a terrestrial planet ($R_p = 1.289^{+0.019}_{-0.014} R_\oplus$, $M_p = 2.770^{+0.076}_{-0.073} M_\oplus$) recently discovered by TESS orbiting an M3.5 dwarf (Trifonov

et al. 2021). At a distance of 8.0756 pc, it is the third-closest known transiting exoplanet system to host a terrestrial exoplanet, and its high emission spectroscopy metric ($\text{ESM} = 21$, Kempton et al. 2018) makes it a prime target for *JWST* observations. Recent X-ray and UV observations of the host star Gl 486 indicate that Gl 486b may have been able to retain an atmosphere with a reasonable initial volatile inventory (Diamond-Lowe et al. 2024). However, despite appearing relatively inactive at optical wavelengths (Caballero et al. 2022), it was also observed to have high-energy XUV flares (Diamond-Lowe et al. 2024). These recent observations also used an age-activity relationship to place a lower limit of 6.6 Gyr on the age of the host star Gl 486.

The transmission spectrum of Gl 486b was observed with *JWST* NIRSpec/G395H between $3 - 5 \mu\text{m}$ (Moran et al. 2023). However, these observations were unable to definitively determine whether the planet had an atmosphere, as the transmission spectrum was consistent with either a water-rich atmosphere or an airless body with a spectrum affected by stellar contamination.

In this paper we present the secondary eclipse spectrum of Gl 486b observed using *JWST*’s Mid-Infrared Instrument (MIRI). We describe our observations and data reduction in Section 2, including an analysis of archival data to precisely constrain the stellar parameters. We describe the calculation of the observed broadband dayside temperature and compare it to expectations for atmospheres and airless bodies in Section 3. In Section 4, we compare the resulting spectra to atmosphere forward models and discuss our result in the context of other observations of M-Earths near the Cosmic Shoreline. Finally, we conclude in Section 6.

2. OBSERVATIONS AND DATA REDUCTION

We observed two secondary eclipses of Gl 486b with *JWST*/MIRI using the Low Resolution Spectroscopy (LRS, Kendrew et al. 2015) Time Series Observation mode, which covers wavelengths from $5 - 12 \mu\text{m}$. The observations were taken on May 29 and June 1, 2023, as part of program GO 1743 (PI Mansfield)¹. Each observation consisted of a single 4.6-hr exposure with 14,810 integrations and 6 groups/integration. The peak pixel counts were $\approx 58,600$ DN ($\approx 86\%$ full well).

We applied two independent data reduction pipelines, SPARTA and Eureka!, to ensure reproducible results.

¹ All of the data presented in this paper were obtained from the Mikulski Archive for Space Telescopes (MAST) at the Space Telescope Science Institute. The specific observations analyzed can be accessed via <http://dx.doi.org/10.17909/3tqz-y166>. The data behind the figures can be found on Zenodo (Weiner Mansfield et al. 2024).

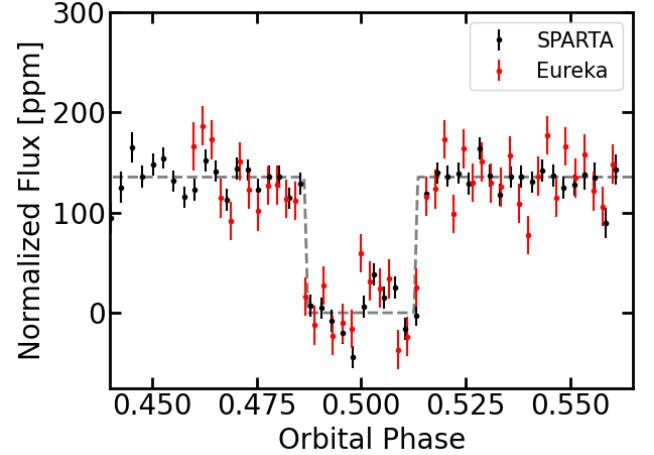


Figure 1. White light curves for both the SPARTA (black) and Eureka! (red) reductions of observations of Gl 486b. The dashed gray line shows the best fit eclipse depth from the SPARTA reduction.

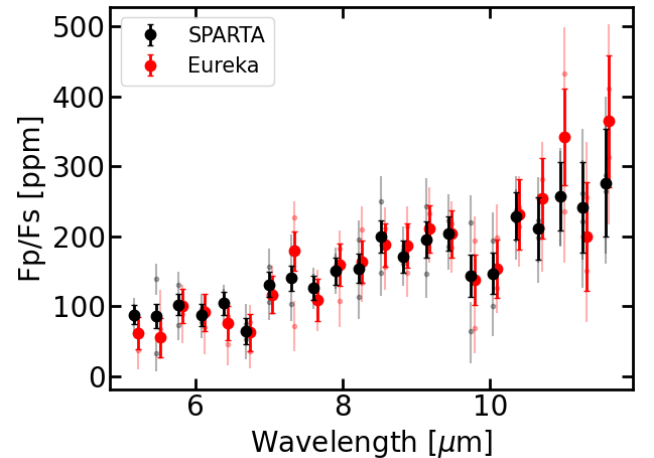


Figure 2. MIRI/LRS eclipse spectra of Gl 486b from the reductions with SPARTA (black) and Eureka! (red). Thin points show results from the two individual eclipses, and thick points show weighted averages of both eclipses combined. The two data reductions are offset slightly in wavelength for clarity. Both independent reductions of both eclipses are in good agreement with each other.

Figures 1 and 2 and Table 1 shows resulting eclipse spectra. The two methods showed consistent white light and spectroscopic eclipse depths within 1σ .

2.1. SPARTA

SPARTA is a completely independent *JWST* data reduction package that does not use any code from any other pipeline, including the standard *JWST* pipeline. It was first introduced in Kempton et al. (2023), and subsequently used in several data analyses (e.g. Bell

Wavelength Range [μm]	SPARTA Eclipse Depth [ppm]	Eureka! Eclipse Depth [ppm]
5.06 – 5.365	88 ± 14	62 ± 23
5.365 – 5.67	86 ± 17	55 ± 28
5.67 – 5.975	102 ± 15	100 ± 25
5.975 – 6.28	87 ± 16	91 ± 27
6.28 – 6.585	104 ± 17	76 ± 25
6.585 – 6.89	64 ± 19	62 ± 26
6.89 – 7.195	131 ± 18	117 ± 27
7.195 – 7.5	140 ± 18	179 ± 28
7.5 – 7.805	126 ± 17	109 ± 30
7.805 – 8.11	150 ± 20	160 ± 30
8.11 – 8.415	154 ± 21	163 ± 30
8.415 – 8.72	199 ± 23	188 ± 31
8.72 – 9.025	171 ± 23	187 ± 32
9.025 – 9.33	195 ± 26	210 ± 34
9.33 – 9.635	204 ± 25	203 ± 34
9.635 – 9.94	143 ± 30	138 ± 36
9.94 – 10.245	147 ± 30	153 ± 42
10.245 – 10.55	229 ± 34	231 ± 50
10.55 – 10.855	211 ± 44	254 ± 58
10.855 – 11.16	257 ± 49	343 ± 69
11.16 – 11.465	241 ± 65	200 ± 77
11.465 – 11.77	276 ± 77	365 ± 94
5.06 – 11.77	135.5 ± 4.9	133.7 ± 6.6

Table 1. Secondary eclipse spectra from both data reductions. The **SPARTA** reduction is the primary one used for analysis, while the **Eureka!** one is included for completeness. The last line lists the broadband eclipse depths.

et al. 2022; Zhang et al. 2024). This paper most closely follows the methodology in Zhang et al. (2024) (see their Appendix A). A brief summary follows.

First, we perform nonlinearity correction, dark subtraction, multiplication by the gain (assumed to be 3.1 electrons/DN), two rounds of up-the-ramp fitting to take out uncorrected nonlinearities, and flat fielding. The two rounds of fitting are meant to take out uncorrected non-linearities: we discard the last group in the first round of fitting, obtain the median residuals across all integrations, add the residuals to the original data, and repeat the up-the-ramp fit.

Afterwards, we remove the background at each wavelength (corresponding to a column, since we rotate the image 90 degrees) by subtracting the median of rows 10:25 and -25:-10 (Python indexing convention) for each column.

Using these background-removed images, we calculate a median image across all integrations, and use it as a

template to calculate the position offset of the trace in each integration in both the x and y directions.

Using the previously calculated median image to generate a spatial profile, we use optimal extraction to extract a spectrum for each integration. We use an extraction half-width of 5 pixels, and reject pixels more than 5σ away from the model image as outliers.

The spectra for each integration are gathered into one pickle file. Integrations that are $> 4\sigma$ outliers in the white light curve are rejected, while $> 4\sigma$ outliers in the unbinned spectroscopic light curves are repaired via interpolation.

Finally, we use the Markov chain Monte Carlo (MCMC) package **emcee** to fit the white light curve (5–12 μm) with an eclipse model and a systematics model after trimming the first 30 minutes (1616 integrations) of data. The free parameters are the eclipse time, eclipse depth, normalization factor, exponential ramp parameters (amplitude and timescale), slope with time, linear detrending parameters with x and y position, and an error inflation factor. The period, R_p/R_s , a/R_s , and inclination are fixed to the “weighted mean” values from the FIREFLY reduction of NIRSpec/G395H transit data (Moran et al. 2023). The two eclipse times were 60093.3530 ± 0.0002 and 60096.2874 ± 0.0002 (BMJD), which are 12 ± 15 s and 22 ± 15 s later than the transit time plus half the period – fully consistent with zero eccentricity when the 17 s light travel time is subtracted out.

To fit the spectroscopic light curves, we fix the eclipse time to 60093.3530 (BMJD_{TDB}) for the first visit and to that value plus twice the period for the second visit. Other system parameters were also fixed to the same values as for the white light curve. The systematics model is identical to the one we used for the white light curve: a linear trend with time, x, and y, multiplied by an exponential ramp, all multiplied by a normalization factor. We use **emcee** (Foreman-Mackey et al. 2013) to simultaneously fit for the eclipse depth, the systematics parameters, and the error inflation for each wavelength bin, after trimming the first 30 minutes of data. We divide the bandpass into 22 wavelength bins, spanning 5.060 to 11.770 μm in 0.305 μm intervals. This binning scheme was chosen to mitigate the “shadowed region” effect (seen in visit 2, but not evident in visit 1), because the reddest 4 bins (between 10.55 and 11.77 μm) perfectly span this region.

2.2. Eureka!

The second data reduction was performed with version 0.10 of the **Eureka!** pipeline (Bell et al. 2022). **Eureka!** is divided into five stages. Stages 1 and 2 use the stan-

standard JWST pipeline to convert from ramp data to slopes and perform calibrations such as flat fielding and unit conversion. Stage 3 extracts spectra from 2D images, Stage 4 creates binned spectroscopic light curves, and Stage 5 fits the data with a **batman** model for astrophysical flux (Kreidberg 2015) and systematic models.

We used the standard **Eureka!** set-up described in Bell et al. (2022), except for the following changes. In Stage 1, we skipped the jump step, as it can introduce noise for observations with a small number of groups. We also assumed a gain of 3.1 electrons/DN, which has been shown to be consistent with on-sky observations (Kempton et al. 2023). In Stage 2, we skipped the photometric flux calibration step to improve estimation of uncertainties. In Stage 3, we extracted the spectrum via optimal extraction (Horne 1986) from a window with a half-width of 6 pixels centered on the location of the spectral trace. We rotated the MIRI spectra so that rows were along the dispersion direction and subtracted the background by fitting a constant column-by-column to the region more than 14 pixels away from the spectral trace on either side. We used a 5σ threshold for outlier rejection during background subtraction and a 10σ threshold while fitting the median image spatial profile. In Stage 4, we corrected for drift along the direction of the spectral trace, as discussed in more detail below. We also performed 10σ sigma clipping on the binned 1D time series.

In Stage 5, we fit the data with a model for the secondary eclipse and a visit-long polynomial systematics trend. We clipped the first 3234 integrations from the beginning of each observation to remove a visible ramp. For the observations taken on May 29 and June 1, we used a zeroth-order and first-order polynomial, respectively. For the June 1 eclipse, the planet-to-star radius ratio (r_p/r_s), period (p), inclination (inc), and eccentricity (ecc) were fixed to the best-fit values from the joint stellar and planetary parameter fit described in Section 2.3. The mid-eclipse time (T_{mid}) and semi-major axis to stellar radius ratio (a/r_s) were free parameters in the white light curve fit then fixed to the best-fit value for the spectroscopic light curve fits. The eclipse depth (F_p/F_s), polynomial coefficients (c_0 and c_1), and a scaling parameter to account for a different level of noise than the Stage 3 prediction ($mult$) were allowed to vary freely in both the white light and spectroscopic fits. The May 29 observation had a higher level of scatter, as described below, so for this fit we fixed a/r_s and T_{mid} to the best-fit values from the June 1 white light curve. The other parameters were treated in the same manner as for the June 1 observation. We estimated the parameters with an MCMC fit using the **emcee** package

(Foreman-Mackey et al. 2013), with 200 walkers, 3500 steps, and a 350-step burn-in.

The observations taken on May 29 showed greater drift in the position of the spectral trace. We first attempted to correct for this by adding free parameters to decorrelate against the x and y positions and widths of the spectral trace, similar to the SPARTA data reduction. However, this decorrelation was unsuccessful in removing the drift noise and left behind approximately hour-long changes in the measured flux of ≈ 100 ppm, at a similar level as the secondary eclipse itself. We additionally tested decorrelating against the x and y positions recorded from SPARTA, which were not identical to the x and y positions recorded by **Eureka!**, but found that this also left structured noise on the order of 100 ppm. We instead opted to use the drift correction built into Stage 4 of **Eureka!**, which cross-correlates spectra to determine the relative drift of each integration. We used a 5 pixel half-width, although we found similar results with many different parameters for the drift correction. In all cases, using **Eureka!**'s drift correction removed the correlated noise but inflated the scatter in the fluxes such that the light curve depths had uncertainties a factor of ≈ 5.5 larger than those measured during the June 1 visit. The **Eureka!** spectrum obtained from averaging both visits therefore had larger error bars than the SPARTA analysis but, as shown in Figures 1 and 2, measured consistent eclipse depths to within 1σ .

2.3. Stellar Parameter Estimation

Correctly translating a measured secondary eclipse depth into a planetary temperature relies on precise knowledge of stellar and planetary parameters such as the stellar effective temperature and semi-major axis. Additionally, expected values of the derived planetary temperature for an airless body or a body with an atmosphere are determined from a global energy balance (Koll et al. 2019), so understanding whether the derived temperature is consistent with an atmosphere also requires precise stellar parameters. Therefore, we used EXOFASTv2 (Eastman et al. 2019), following the procedure of Mahajan et al. (2024) to perform a joint fit of several different observations of Gl 486b and precisely constrain stellar and planetary parameters. We simultaneously fit the white light curves from the two secondary eclipses presented in this study, white light curves from two transits taken with JWST/NIRSpec (Moran et al. 2023, with separate fits for the NRS1 and NRS2 detectors), and data from Sector 23 (March - April 2020) of the Transiting Exoplanet Survey Satellite. We used data from Sector 23 because it was the earliest available observation of Gl 486b with TESS, which maximized the

time baseline and therefore provided the tightest constraint on the ephemeris.

As was done in [Xue et al. \(2024\)](#), we modeled ramps for the *JWST* data. The best-fit parameters are included in Appendix A in Table 2. Using the precisely measured stellar density, the [Mann et al. \(2019\)](#) stellar mass, and the bolometric flux from the spectral energy distribution, the joint fit increased the precision on the stellar radius and stellar effective temperature by $3.5\times$ and $2\times$, respectively, compared to the previous best fit ([Caballero et al. 2022](#)). Additionally, both of those parameters, as well as the stellar mass, r_p/r_s , and a/r_s , were consistent within 1σ with previous fits ([Caballero et al. 2022](#); [Moran et al. 2023](#)). While the previous fit assumed a circular orbit with zero eccentricity, our fit was able to precisely constrain the eccentricity to $0.00086^{+0.0016}_{-0.00043}$, which is consistent with zero given the Lucy-Sweeney bias on the eccentricity, which is a positive definite quantity ([Lucy & Sweeney 1971](#)). The MIRI/LRS white light eclipse depth obtained from the EXOFASTv2 fit is $133.3^{+5.0}_{-4.9}$ ppm, which is consistent to within 1σ with the white light depths derived from the SPARTA and Eureka! data reductions.

3. DAYSIDE TEMPERATURE CALCULATION

We follow the method outlined in [Xue et al. \(2024\)](#) to convert the white light eclipse depth from the EXOFASTv2 fit to a planetary dayside temperature. Briefly, we took the planet-to-star flux ratio (F_p/F_s), planet-to-star radius ratio (R_p/R_s), stellar effective temperature (T_s), stellar metallicity ($[M/H]$), and stellar gravity ($\log g$) from each sample in the Markov Chain Monte Carlo fit performed by EXOFASTv2. We then obtained a stellar spectrum by interpolating from a PHOENIX grid ([Allard et al. 2012](#)) to the correct T_s , $[M/H]$, and $\log g$ using the python package `pysynphot` ([STScI Development Team 2013](#)). We tested performing the same fit with an interpolated SPHINX model ([Iyer et al. 2023](#)) and found consistent results. We convolved the stellar spectrum with a Gaussian kernel to broaden it to the resolution of MIRI/LRS and used it to calculate the photon flux from the planet in each sample following the equation

$$\frac{F_p}{F_s} = \left(\frac{R_p}{R_s}\right)^2 \cdot \frac{\int \frac{\pi \cdot B_p(T_p, \lambda)}{hc/\lambda} \cdot W_\lambda d\lambda}{\int \frac{M_s(T_s, \log g, [M/H], \lambda)}{hc/\lambda} \cdot W_\lambda d\lambda}, \quad (1)$$

where $B_p(T_p, \lambda)$ is the planet flux (assuming it acts as a blackbody), $M_s(T_s, \log g, [M/H], \lambda)$ is the interpolated stellar spectrum, and W_λ is the MIRI/LRS throughput. We then invert Equation 1 to convert the photon flux to a planetary temperature for each sample.

Figure 3 shows a pairs plot for the stellar parameters and dayside temperature. We derive a planetary dayside temperature of $T_p = 865 \pm 14$ K. This calculation assumes that the MIRI/LRS eclipse depth is a good estimate for bolometric flux, and thus that the planet roughly emits as a blackbody. We make these assumptions because a planet at the temperature of Gl 486b will emit $\approx 45\%$ of its flux in the LRS bandpass and realistic surfaces emit close enough to a blackbody that this estimate approximates the true dayside temperature well. For example, if the true albedo were 0.1 higher than the albedo we infer from this infrared measurement (a typical difference between the inferred and true bond albedo, [Mansfield et al. 2019](#); [Whittaker et al. 2022](#)), our dayside temperature would only change by 15 K, or about 1σ .

We neglect thermal beaming, which may result from (e.g.) surface roughness effects ([Spencer 1990](#)), and which can raise the observed low-phase-angle brightness temperature of atmosphere-free bodies above $T_{p,max}$ ([Emery et al. 1998](#)). This does not affect our conclusion that the atmosphere is probably very thin or absent.

The dayside temperature will depend on both heat redistribution and albedo ([Cowan & Agol 2011](#)), and the derived joint constraint can be compared to expected values for the heat redistribution and albedo for atmospheres to determine the likelihood that Gl 486b has an atmosphere ([Koll et al. 2019](#); [Mansfield et al. 2019](#)). Following [Xue et al. \(2024\)](#), we calculate the temperature ratio \mathcal{R} , which compares the derived dayside temperature to the maximum possible temperature for a zero-albedo, zero heat redistribution, smooth bare rock ($T_{p,max}$). We calculate \mathcal{R} using the equation

$$\begin{aligned} \mathcal{R} &= \frac{T_{p,dayside}}{T_{p,max}} \\ &= \frac{T_{p,dayside} \sqrt{a/R_s}}{\left(\frac{2}{3}\right)^{\frac{1}{4}} T_s}, \end{aligned} \quad (2)$$

where a is the semi-major axis and R_s is the stellar radius. We derive a value of $\mathcal{R} = 0.97 \pm 0.01$.

We determine which albedo and heat redistribution values are consistent with the derived \mathcal{R} using the equation

$$\mathcal{R} = \left(\frac{2}{3}\right)^{-\frac{1}{4}} \cdot (1 - A_B)^{\frac{1}{4}} \cdot \left(\frac{2}{3} - \frac{5}{12}\epsilon\right)^{\frac{1}{4}}, \quad (3)$$

where A_B is the Bond albedo, ϵ is the heat redistribution efficiency, and the factor of $\left(\frac{2}{3}\right)^{-1/4}$ is a normalization to ensure that $\mathcal{R} = 1$ for the case where there is zero albedo and zero heat redistribution ($A_B = \epsilon = 0$, [Cowan & Agol 2011](#)).

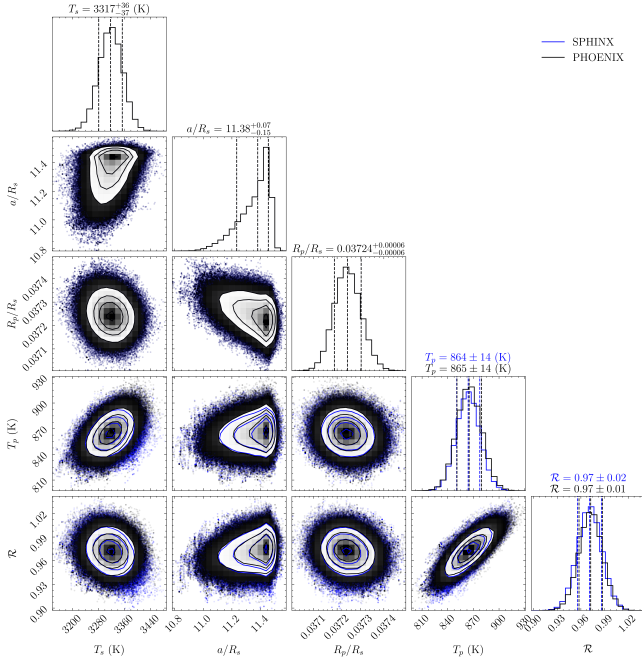


Figure 3. Pairs plot for the best-fit parameters from the joint stellar and planetary fit described in Section 2.3, as well as the derived temperature ratio (\mathcal{R}) described in Section 3. Black and blue plots show results using a PHOENIX (Allard et al. 2012) and SPHINX (Iyer et al. 2023) stellar model, respectively. Off-diagonal plots show 2D posterior probabilities for pairs of parameters, with dark, medium, and light shading showing 1, 2, and 3 σ confidence intervals. On-diagonal plots show marginalized posterior probability distributions for each individual parameter.

Figure 4 shows the joint constraint on albedo and heat redistribution obtained from the dayside brightness temperature of Gl 486b. Figure 4 compares this constraint with values for the solar system terrestrial planets and the Moon. We assume albedos of $A_B = 0.11, 0.119, 0.75, 0.306$, and 0.250 for the Moon, Mercury, Venus, Earth, and Mars, respectively. The primary global temperature difference for the fast-rotating solar system bodies is the equator-to-pole temperature difference, rather than the dayside-to-nightside temperature difference that is used to calculate the heat redistribution factor for slow-rotating hot exoplanets. Therefore, following Cowan & Agol (2011), we derive the heat redistribution factor for the solar system bodies using the equation

$$\varepsilon = \frac{8/3}{(T_{\text{equator}}/T_{\text{pole}})^4 + 5/3}, \quad (4)$$

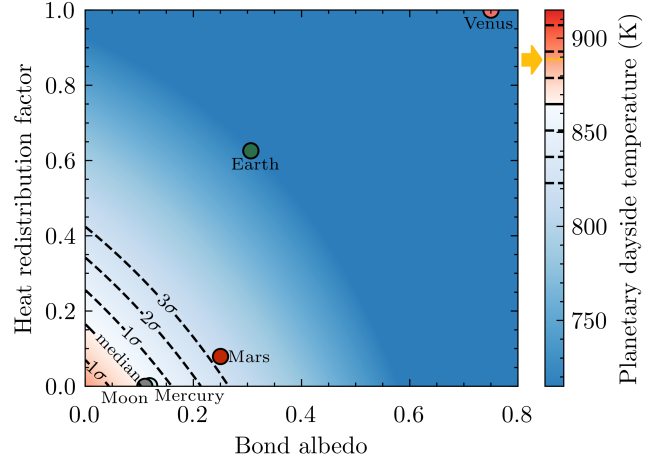


Figure 4. Contour plot showing the planetary dayside temperature of Gl 486b as a function of Bond albedo (A_B) and heat redistribution factor (ε). Note that T_s , a/R_s and R_p/R_s are identical. They are drawn from each sample in the EXOFASTv2 MCMC fitting. The solid line shows a contour of the median planetary temperature inferred for Gl 486b, and the surrounding dotted lines show 1 σ , 2 σ , and 3 σ intervals. The yellow arrow on the colorbar shows the maximum dayside temperature predicted for Gl 486b if it had zero Bond albedo and no heat redistribution. Gray, light blue, red, green, and yellow dots show approximate values for the solar system bodies Moon, Mercury, Mars, Earth, and Venus, respectively. Our observations of Gl 486b are most consistent with airless bodies like the Moon and Mercury that have slight non-zero albedos, and it is highly inconsistent with a thick Earth-like or Venus-like atmosphere.

where T_{equator} and T_{pole} are the mean equator and pole temperatures, respectively.

We find that our observations of Gl 486b are most consistent with airless bodies with small non-zero albedos of $A_B \approx 0.1$, similar to the Moon and Mercury. Although the observations are consistent to within $\approx 3\sigma$ with the presence of a thin atmosphere such as that found on Mars, they are highly inconsistent with thick, Earth- or Venus-like atmospheres.

4. COMPARISON TO FORWARD MODELS

Although our results show that the data are strongly inconsistent with the presence of a thick atmosphere, we compared a set of forward models to our data to determine which types of atmospheres would still be allowable. We followed the methods of Whittaker et al. (2022) and Ih et al. (2023) to use HELIOS to construct forward modeled thermal emission spectra for Gl 486b. We used a SPHINX stellar model (Iyer et al. 2023, updated May 30th, 2024) for the input stellar flux. We modeled atmospheres with surface pressures of $10^{-4} - 100$ bar. We modeled atmospheres with pure H_2O , pure CO_2 , and

the same ratio of gases as Earth’s atmosphere. We also modeled atmospheres including 1 ppm, 100 ppm, or 1 % of either H_2O or CO_2 , with the rest of the atmosphere filled with O_2 as a stand-in for a background gas with no spectral features observable at MIRI/LRS wavelengths. Finally, we modeled the secondary eclipse depth for bare rock planets of the surface types described in [Hu et al. \(2012\)](#).

Figure 5 shows the best fitting forward models compared to the observed eclipse spectrum. Reduced chi squared values for the models quoted in this figure are calculated only from taking into account the error bars on the observed eclipse depths, not errors on the stellar and orbital parameters which could change the overall eclipse depths in the forward models themselves. Low-albedo bare rock surfaces (basalt, oxidized iron, ultramafic, or metal-rich rocks) are relatively consistent with the observed spectrum, with reduced chi squared values between $1.19 \leq \chi^2_\nu \leq 1.35$. All other forward models with $\chi^2_\nu \leq 1.5$ are shown in Figure 5. The only atmosphere models whose fits are comparable in reduced chi squared with the bare rock models are those with small amounts of H_2O or CO_2 in relatively thin atmospheres. Figure 5 also shows the best-fit blackbody to the data, which had a dayside temperature of 824 ± 12 K and achieved a reduced chi-squared of 1.07.

The only O_2 -rich atmospheres which were consistent with the data to within a reduced chi squared of 4 had surface pressures of 1 – 10 bar and < 100 ppm H_2O or CO_2 in them. Additionally, in order to have a reduced chi squared of less than 4, a pure H_2O , pure CO_2 , or Earth-like atmosphere would have to have a surface pressure of < 0.1 bar, $< 10^{-4}$ bar, and < 0.01 bar, respectively. The data strongly disfavor thicker atmospheres and/or those with larger concentrations of H_2O or CO_2 .

5. DISCUSSION

As discussed in Section 4, our observed emission spectrum is most consistent with either airless bodies or atmospheres with modest surface pressures and small concentrations of infrared absorbers such as H_2O and CO_2 . Our observations are highly inconsistent with atmospheres thicker than ≈ 1 bar with more than ≈ 100 ppm of H_2O or CO_2 . [Moran et al. \(2023\)](#) observed Gl 486b in transit with *JWST*/NIRSpec between 3 – 5 μm . Their resulting transmission spectrum showed a slope toward the shorter wavelengths that could be described well by either a water-rich planetary atmosphere or an airless planet affected by unocculted starspots and the Transit Light Source Effect ([Rackham et al. 2018](#)). [Moran et al. \(2023\)](#) performed a retrieval for the water-rich case

and found it preferred a composition with $> 10\%$ water. Our eclipse spectrum is inconsistent with a $> 10\%$ water atmospheric composition, regardless of the exact composition of the remaining 90% of the atmosphere, because such an atmosphere would be expected to have much more prominent water absorption features in the MIRI/LRS bandpass.

[Diamond-Lowe et al. \(2024\)](#) observed the host star Gl 486b at X-ray and UV wavelengths and found multiple high-energy flares in a short time period. This result suggests that, although Gl 486 presents as relatively inactive at optical wavelengths, it may nonetheless be active enough in the UV to efficiently strip Gl 486b of any atmosphere. Given the inconsistency in water mass fraction for a potential atmosphere between our emission spectrum and the transit observations of [Moran et al. \(2023\)](#), and the potential for Gl 486’s activity to strip thin atmospheres over its ≥ 6.6 -Gyr lifetime ([Diamond-Lowe et al. 2024](#)), we find that our observations are more consistent with an airless planet.

Our observation of Gl 486b’s thermal emission resulted in the most precise constraint yet on the day-side temperature of a terrestrial planet (for example, *JWST*/MIRI observations of TRAPPIST-1b and *Spitzer* observations of LHS 3844b had 1σ dayside temperature errors of 26 K and 40 K, respectively). Therefore, although we did not detect strong evidence for an atmosphere, we can use this precise measurement to constrain the position of the Cosmic Shoreline for M-Earths. Figure 6 plots the escape velocity and cumulative XUV flux for the solar system terrestrial planets and the population of M-Earths observed with *JWST* ([Greene et al. 2023](#); [Zieba et al. 2023](#); [Zhang et al. 2024](#); [Xue et al. 2024](#)) or *Spitzer* ([Kreidberg et al. 2019](#); [Crossfield et al. 2022](#)), assuming the scaling relationship for cumulative XUV flux from [Zahnle & Catling \(2017\)](#). The blue line shows the Cosmic Shoreline assuming that Mars, which retains a very thin atmosphere, resides exactly along the shoreline ([Zahnle & Catling 2017](#)). Theory predicts that bodies to the upper left of this dividing line will lose their atmospheres to XUV-driven escape, while those to the lower right will retain their atmospheres.

Our result suggests that future observations of M-Earths may need to probe closer to the Cosmic Shoreline to successfully detect thick atmospheres. However, the current sample of observed M-Earths is relatively small and heavily biased towards highly irradiated objects. Future surveys, such as the 500 hour DDT program to observe M-Earths with *JWST* ([Redfield et al. 2024](#)), will increase the size of this sample and improve our understanding of the Cosmic Shoreline for M-Earths.

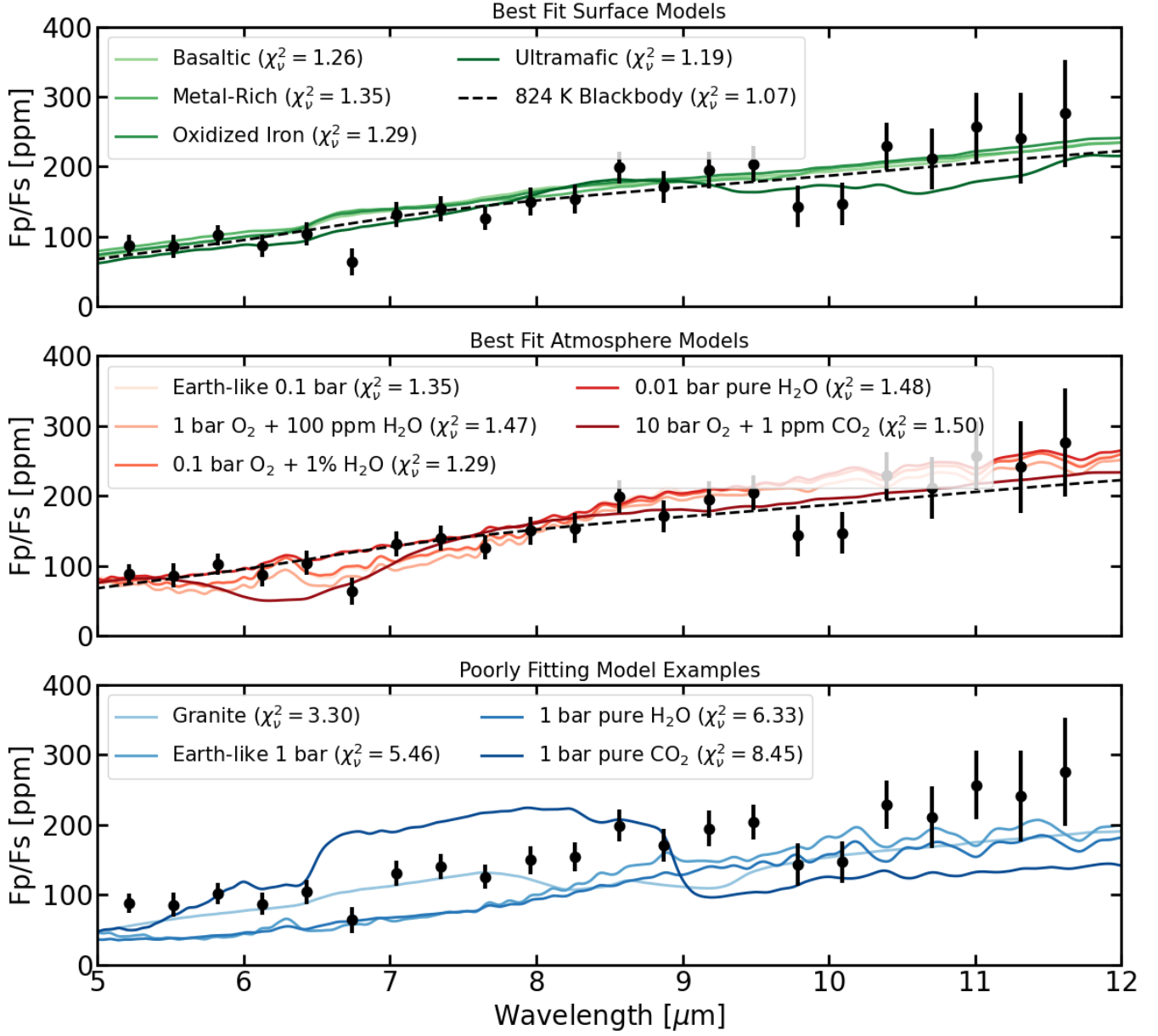


Figure 5. Comparison of the eclipse spectrum of Gl 486b (black points) with a variety of atmosphere and bare rock forward models. Top and middle panels show all bare rock and atmosphere models that have a reduced chi squared of ≤ 1.5 , respectively, assuming the number of degrees of freedom equals the number of data points. The bottom panel shows a selection of bare rock and atmosphere models which give worse fits to the data. The only atmospheres as consistent with our data as the bare rock models have relatively low surface pressures and/or small concentrations of the infrared absorbers H_2O and CO_2 .

6. CONCLUSIONS

We observed two secondary eclipses of the hot terrestrial exoplanet Gl 486b with *JWST*/MIRI+LRS between 5 – 12 μm . We jointly modeled these observations with previous *JWST*/NIRSpec+G395H and *TESS* transits to derive precise constraints on the stellar and planetary parameters. Based on these constraints, we derived a broadband dayside temperature of $T_p = 865 \pm 14$ K and a temperature ratio of $\mathcal{R} = \frac{T_{p,\text{dayside}}}{T_{p,\text{max}}} =$

0.97 ± 0.01 . While this value could be consistent with either an airless body with a small, non-zero albedo (i.e., the Moon or Mercury) or a thin atmosphere, it is inconsistent with Earth- or Venus-like atmospheres. In light of the previous transit observations of Gl 486b with *JWST*/NIRSpec (Moran et al. 2023) and the likelihood of a thin atmosphere escaping over the ≥ 6.6 -Gyr lifetime of Gl 486 (Diamond-Lowe et al. 2024), we conclude that Gl 486b is most likely an airless rock. However, our measurement of the dayside temperature is the most

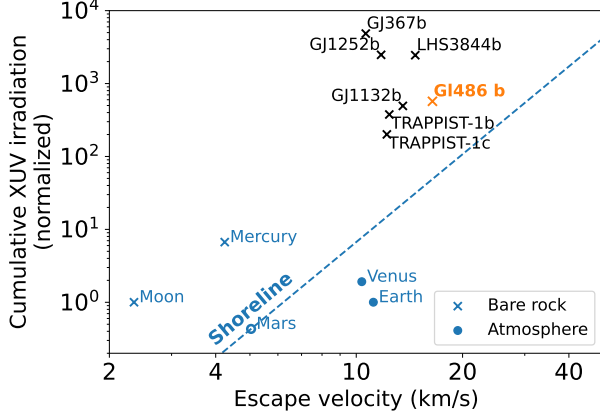


Figure 6. The Cosmic Shoreline (dashed blue line; Zahnle & Catling 2017), compared to select rocky bodies in the Solar System (blue) and in M Dwarf systems (black, orange). The plotted Cosmic Shoreline is a relationship between escape velocity and normalized cumulative XUV irradiation that is empirically observed in the Solar System. For exoplanets, crosses indicate planets whose observations rule out thick atmospheres and are consistent with no atmosphere. For Solar System bodies, crosses, open circles, and filled circles indicate bodies with no atmosphere, thin ($P < 1$ bar) atmospheres, and thick ($P \geq 1$ bar) atmospheres, respectively. Gl 486b is the second-closest exoplanet to the shoreline probed for an atmosphere so far, after TRAPPIST-1c.

precise of any *JWST* thermal emission observations of terrestrial planets, which places a strong constraint on the position of the Cosmic Shoreline. This tight constraint can provide guidance for future searches for terrestrial exoplanet atmospheres with *JWST*.

This work is based on observations with the NASA/ESA/CSA *JWST*. The data were obtained from the Mikulski Archive for Space Telescopes at the Space Telescope Science Institute (STScI), which is operated by the Association of Universities for Research in Astronomy, Incorporated, under NASA contract NAS5-03127. These observations are associated with program #1743. Support for this program was provided through a grant from STScI. M.W.M. acknowledges support through the NASA Hubble Fellowship grant HST-HF2-51485.001-A awarded by STScI. M.Z. acknowledges support through the 51 Pegasi b fellowship program awarded by the Heising-Simons Foundation. J. I. and E. M.-R. K. acknowledge support from the AETHeR Matter-to-Life program, funded by the Alfred P. Sloan Foundation under grant G202114194. Work by A.S.M. and J.D.E. was funded by NASA ADAP 80NSSC19K1014. We thank the anonymous reviewer for their helpful comments.

Facilities: *JWST*/MIRI

Software: Eureka! (Bell et al. 2022), SPARTA (Kempton et al. 2023), batman (Kreidberg 2015), astropy (Astropy Collaboration et al. 2013, 2018, 2022), matplotlib (Hunter 2007), numpy (Harris et al. 2020), pysynphot (STScI Development Team 2013), scipy (Virtanen et al. 2021), ExoFASTv2 (Eastman et al. 2019), HELIOS (Malik et al. 2017, 2019b,a; Whittaker et al. 2022)

APPENDIX

A. STELLAR PARAMETERS

Table 2. Median values and 68% confidence interval for the EXOFASTv2 fit to *JWST* and *TESS* observations of Gl 486b.

Parameter	Description	Values
Stellar Parameters:		
M_*	Mass (M_\odot)	$0.3120^{+0.0070}_{-0.0069}$
R_*	Radius (R_\odot)	$0.3243^{+0.0044}_{-0.0034}$
$R_{*,SED}$..	Radius ¹ (R_\odot)	$0.3573^{+0.0054}_{-0.0061}$
L_*	Luminosity (L_\odot)	$0.01151^{+0.00047}_{-0.00046}$

Table 2 continued

Table 2 (*continued*)

Parameter	Description	Values
F_{Bol}	Bolometric Flux (cgs)	$5.64 \pm 0.23 \times 10^{-9}$
ρ_*	Density (cgs)	$12.95^{+0.25}_{-0.50}$
$\log g$	Surface gravity (cgs)	$4.9111^{+0.0068}_{-0.011}$
T_{eff}	Effective temperature (K)	3317^{+36}_{-37}
$T_{\text{eff,SED}}$	Effective temperature ¹ (K)	3197^{+23}_{-21}
[Fe/H]	Metallicity (dex)	$-0.15^{+0.13}_{-0.12}$
K_S	Absolute Ks-band mag (mag)	6.823 ± 0.020
k_S	Apparent Ks-band mag (mag)	6.359 ± 0.020
A_V	V-band extinction (mag)	$0.034^{+0.029}_{-0.024}$
σ_{SED}	SED photometry error scaling	$1.56^{+0.63}_{-0.37}$
ϖ	Parallax (mas)	123.830 ± 0.034
d	Distance (pc)	8.0756 ± 0.0022
Planetary Parameters:		b
P	Period (days)	$1.46712127^{+0.00000031}_{-0.00000035}$
R_P	Radius (R_{\oplus})	$1.289^{+0.019}_{-0.014}$
M_P	Mass (M_{\oplus})	$2.770^{+0.076}_{-0.073}$
T_C	Observed Time of conjunction ² (BJD _{TDB})	$2459691.128107^{+0.000060}_{-0.000054}$
T_C	Model Time of conjunction ^{2,3} (TJD _{TDB})	$2459691.128008^{+0.000060}_{-0.000054}$
T_T	Model time of min proj sep ^{3,4,5} (TJD _{TDB})	$2459939.071503^{+0.000010}_{-0.000011}$
T_0	Obs time of min proj sep ^{4,6,7} (BJD _{TDB})	$2459939.071602 \pm 0.000010$
a	Semi-major axis (AU)	0.01714 ± 0.00013
i	Inclination (Degrees)	$89.39^{+0.41}_{-0.42}$
e	Eccentricity	$0.00086^{+0.0016}_{-0.00043}$
ω_*	Arg of periastron (Degrees)	14^{+62}_{-85}
$\dot{\omega}_{GR}$	Computed GR precession ($^{\circ}$ /century)	4.832 ± 0.072
T_{eq}	Equilibrium temp ⁸ (K)	$696.3^{+7.2}_{-7.3}$
τ_{circ}	Tidal circ timescale (Gyr)	$2.87^{+0.13}_{-0.19}$
K	RV semi-amplitude (m/s)	$3.389^{+0.076}_{-0.075}$
R_P/R_*	Radius of planet in stellar radii	$0.037244^{+0.000059}_{-0.000056}$
a/R_*	Semi-major axis in stellar radii	$11.380^{+0.074}_{-0.15}$
δ	$(R_P/R_*)^2$	$0.0013871^{+0.0000044}_{-0.0000042}$
δ_{MIRILRS}	Transit depth in MIRI/LRS (frac)	$0.00194^{+0.0015}_{-0.00043}$
δ_{NRS1}	Transit depth in NIRSpec/G395H/NRS1 (frac)	$0.001443^{+0.000026}_{-0.000025}$
δ_{NRS2}	Transit depth in NIRSpec/G395H/NRS2 (frac)	$0.001518^{+0.000027}_{-0.000030}$
δ_{TESS}	Transit depth in TESS (frac)	$0.00155^{+0.00020}_{-0.00011}$
τ	In/egress transit duration (days)	$0.001545^{+0.000043}_{-0.000020}$
T_{14}	Total transit duration (days)	$0.042327^{+0.000041}_{-0.000035}$
T_{FWHM}	FWHM transit duration (days)	$0.040775^{+0.000028}_{-0.000027}$
b	Transit impact parameter	$0.120^{+0.080}_{-0.081}$
b_S	Eclipse impact parameter	$0.120^{+0.080}_{-0.081}$

Table 2 *continued*

Table 2 (*continued*)

Parameter	Description	Values
τ_S	In/egress eclipse duration (days)	$0.001546^{+0.000043}_{-0.000021}$
$T_{S,14}$	Total eclipse duration (days)	$0.04234^{+0.00014}_{-0.00011}$
$T_{S,FWHM}$	FWHM eclipse duration (days)	$0.040785^{+0.00013}_{-0.000097}$
$\delta_{S,2.5\mu m}$. .	BB eclipse depth at $2.5\mu m$ (ppm)	1.67 ± 0.11
$\delta_{S,5.0\mu m}$. .	BB eclipse depth at $5.0\mu m$ (ppm)	$31.21^{+0.97}_{-0.94}$
$\delta_{S,7.5\mu m}$. .	BB eclipse depth at $7.5\mu m$ (ppm)	$73.7^{+1.5}_{-1.4}$
ρ_P	Density (cgs)	$6.66^{+0.23}_{-0.29}$
$\log g_P$	Surface gravity (cgs)	$3.194^{+0.012}_{-0.014}$
Θ	Safronov Number	0.00813 ± 0.00021
$\langle F \rangle$	Incident Flux ($10^9 \text{ erg s}^{-1} \text{ cm}^{-2}$)	$0.0533^{+0.0023}_{-0.0022}$
T_S	Observed Time of eclipse ² (BJD _{TDB})	$2459690.39472 \pm 0.00015$
T_S	Model Time of eclipse ^{2,3} (TJD _{TDB})	$2459690.39482 \pm 0.00015$
T_E	Model time of sec min proj sep ^{3,4,5} (TJD _{TDB})	$2460099.72165 \pm 0.00012$
$T_{E,0}$	Obs time of sec min proj sep ^{4,6,7} (BJD _{TDB})	$2460099.72155 \pm 0.00012$
T_P	Time of Periastron (TJD _{TDB})	$2459690.82^{+0.25}_{-0.35}$
T_A	Time of asc node (TJD _{TDB})	$2459692.22857^{+0.00078}_{-0.00054}$
T_D	Time of desc node (TJD _{TDB})	$2459691.49491^{+0.00057}_{-0.00072}$
V_c/V_e	Scaled velocity	$0.9999^{+0.0011}_{-0.0016}$
$e \cos \omega_*$	0.00040 ± 0.00013
$e \sin \omega_*$	$0.0001^{+0.0016}_{-0.0011}$
$M_P \sin i$	Minimum mass (M_J)	$0.00871^{+0.00024}_{-0.00023}$
M_P/M_*	Mass ratio	$2.667^{+0.063}_{-0.062} \times 10^{-5}$
d/R_*	Separation at mid transit	$11.374^{+0.082}_{-0.15}$
P_T	A priori non-grazing transit prob	$0.08465^{+0.0011}_{-0.00060}$
$P_{T,G}$	A priori transit prob	$0.09119^{+0.0012}_{-0.00065}$
P_S	A priori non-grazing eclipse prob	$0.08457^{+0.0011}_{-0.00053}$
$P_{S,G}$	A priori eclipse prob	$0.09111^{+0.0012}_{-0.00057}$
Wavelength Parameters:		
MIRI/LRS		
u_1	Linear limb-darkening coeff	$0.58^{+0.61}_{-0.42}$
u_2	Quadratic limb-darkening coeff	$0.00^{+0.44}_{-0.43}$
δ_S	Measured eclipse depth (ppm)	$133.3^{+5.0}_{-4.9}$
NIRSpec/G395H/NRS1		
u_1	Linear limb-darkening coeff	$0.079^{+0.035}_{-0.034}$
u_2	Quadratic limb-darkening coeff	0.149 ± 0.053
NIRSpec/G395H/NRS2		
u_1	Linear limb-darkening coeff	$0.175^{+0.033}_{-0.037}$
u_2	Quadratic limb-darkening coeff	$-0.033^{+0.055}_{-0.048}$
TESS		
u_1	Linear limb-darkening coeff	$0.21^{+0.21}_{-0.15}$

Table 2 *continued*

Table 2 (*continued*)

Parameter	Description	Values
u_2	Quadratic limb-darkening coeff	$0.34^{+0.25}_{-0.31}$
Telescope Parameters:		
CARMENES		
γ_{rel}	Relative RV Offset (m/s)	-0.07 ± 0.24
σ_J	RV Jitter (m/s)	$1.72^{+0.22}_{-0.20}$
σ_J^2	RV Jitter Variance	$2.95^{+0.82}_{-0.66}$
MAROON-X-Blue		
γ_{rel}	Relative RV Offset (m/s)	0.01 ± 0.11
σ_J	RV Jitter (m/s)	0.61 ± 0.13
σ_J^2	RV Jitter Variance	$0.37^{+0.18}_{-0.14}$
MAROON-X-Red		
γ_{rel}	Relative RV Offset (m/s)	0.039 ± 0.059
σ_J	RV Jitter (m/s)	$0.392^{+0.056}_{-0.052}$
σ_J^2	RV Jitter Variance	$0.153^{+0.047}_{-0.038}$
Transit Parameters:		
TESS UT 2020-03-21 (TESS)		
σ^2	Added Variance	$-2.609^{+0.058}_{-0.057} \times 10^{-7}$
F_0	Baseline flux	1.0000385 ± 0.0000060
JWST UT 2022-12-25 (NIRSpec/G395H/NRS1)		
σ^2	Added Variance	$-2.4^{+5.1}_{-4.9} \times 10^{-10}$
τ_{Ramp}	Exponential Ramp	$0.1321^{+0.0068}_{-0.0062}$
A_{Ramp}	Amp of exp ramp	$0.002000^{+0.000055}_{-0.000050}$
F_0	Baseline flux	$1.0011938^{+0.0000088}_{-0.0000087}$
JWST UT 2022-12-25 (NIRSpec/G395H/NRS2)		
σ^2	Added Variance	$3.6^{+7.4}_{-7.1} \times 10^{-10}$
τ_{Ramp}	Exponential Ramp	$0.0374^{+0.012}_{-0.0077}$
A_{Ramp}	Amp of exp ramp	$9.5 \pm 1.2 \times 10^{-5}$
F_0	Baseline flux	1.000460 ± 0.000012
JWST UT 2022-12-29 (NIRSpec/G395H/NRS1)		
σ^2	Added Variance	$-0.4^{+4.7}_{-4.5} \times 10^{-10}$
τ_{Ramp}	Exponential Ramp	$0.194^{+0.014}_{-0.013}$
A_{Ramp}	Amp of exp ramp	$0.00253^{+0.00012}_{-0.00011}$
F_0	Baseline flux	$1.0011544^{+0.0000082}_{-0.0000081}$
JWST UT 2022-12-29 (NIRSpec/G395H/NRS2)		
σ^2	Added Variance	$0.1^{+6.1}_{-5.9} \times 10^{-10}$
τ_{Ramp}	Exponential Ramp	$0.044^{+0.63}_{-0.021}$
A_{Ramp}	Amp of exp ramp	$-5.5^{+1.6}_{-7.3} \times 10^{-5}$
F_0	Baseline flux	$1.000361^{+0.000014}_{-0.000017}$
JWST UT 2023-05-29 (MIRI/LRS)		

Table 2 *continued*

Table 2 (*continued*)

Parameter	Description	Values
σ^2	Added Variance	$-1.2^{+9.0}_{-8.8} \times 10^{-10}$
τ_{Ramp} . . .	Exponential Ramp	$0.0151^{+0.011}_{-0.0044}$
A_{Ramp} . . .	Amp of exp ramp	$9.7^{+2.5}_{-1.8} \times 10^{-5}$
F_0	Baseline flux	$1.000094^{+0.000020}_{-0.000026}$
C_0	Additive detrending coeff	-0.000555 ± 0.000011
C_1	Additive detrending coeff	$-5.8 \pm 1.2 \times 10^{-5}$
JWST UT 2023-06-01 (MIRI/LRS)		
σ^2	Added Variance	$-2.1^{+9.1}_{-8.9} \times 10^{-10}$
τ_{Ramp} . . .	Exponential Ramp	$0.35^{+0.45}_{-0.24}$
A_{Ramp} . . .	Amp of exp ramp	$0.00039^{+0.00039}_{-0.00020}$
F_0	Baseline flux	$1.0000686^{+0.000012}_{-0.0000080}$
C_0	Additive detrending coeff	$-0.0004216^{+0.000010}_{-0.0000100}$
C_1	Additive detrending coeff	$-3.7 \pm 1.1 \times 10^{-5}$

See Table 3 in [Eastman et al. \(2019\)](#) for a detailed description of all parameters

¹This value ignores the systematic error and is for reference only

²Time of conjunction is commonly reported as the “transit time”

³TJD_{TDB} is the target’s barycentric frame and corrects for light travel time

⁴Time of minimum projected separation is a more correct “transit time”

⁵Use this to model TTVs, e

⁶At the epoch that minimizes the covariance between T_C and Period

⁷Use this to predict future transit times

⁸Assumes no albedo and perfect redistribution

REFERENCES

- Allard, F., Homeier, D., & Freytag, B. 2012, Philosophical Transactions of the Royal Society of London Series A, 370, 2765, doi: [10.1098/rsta.2011.0269](#)
- Astropy Collaboration, Robitaille, T. P., Tollerud, E. J., et al. 2013, A&A, 558, A33, doi: [10.1051/0004-6361/201322068](#)
- Astropy Collaboration, Price-Whelan, A. M., Sipőcz, B. M., et al. 2018, AJ, 156, 123, doi: [10.3847/1538-3881/aabc4f](#)
- Astropy Collaboration, Price-Whelan, A. M., Lim, P. L., et al. 2022, ApJ, 935, 167, doi: [10.3847/1538-4357/ac7c74](#)
- Bell, T., Ahrer, E.-M., Brande, J., et al. 2022, The Journal of Open Source Software, 7, 4503, doi: [10.21105/joss.04503](#)
- Caballero, J. A., González-Álvarez, E., Brady, M., et al. 2022, A&A, 665, A120, doi: [10.1051/0004-6361/202243548](#)
- Cowan, N. B., & Agol, E. 2011, ApJ, 729, 54, doi: [10.1088/0004-637X/729/1/54](#)
- Crossfield, I. J. M., Malik, M., Hill, M. L., et al. 2022, ApJL, 937, L17, doi: [10.3847/2041-8213/ac886b](#)
- Davenport, J. R. A., Becker, A. C., Kowalski, A. F., et al. 2012, ApJ, 748, 58, doi: [10.1088/0004-637X/748/1/58](#)
- Diamond-Lowe, H., King, G. W., Youngblood, A., et al. 2024, arXiv e-prints, arXiv:2407.00165, doi: [10.48550/arXiv.2407.00165](#)
- Dorn, C., & Heng, K. 2018, ApJ, 853, 64, doi: [10.3847/1538-4357/aa9c80](#)

- Eastman, J. D., Rodriguez, J. E., Agol, E., et al. 2019, arXiv e-prints, arXiv:1907.09480, doi: [10.48550/arXiv.1907.09480](https://doi.org/10.48550/arXiv.1907.09480)
- Emery, J. P., Sprague, A. L., Witteborn, F. C., et al. 1998, *Icarus*, 136, 104, doi: [10.1006/icar.1998.6012](https://doi.org/10.1006/icar.1998.6012)
- Foreman-Mackey, D., Hogg, D. W., Lang, D., & Goodman, J. 2013, *PASP*, 125, 306, doi: [10.1086/670067](https://doi.org/10.1086/670067)
- Greene, T. P., Bell, T. J., Ducrot, E., et al. 2023, *Nature*, 618, 39, doi: [10.1038/s41586-023-05951-7](https://doi.org/10.1038/s41586-023-05951-7)
- Harris, C. R., Millman, K. J., van der Walt, S. J., et al. 2020, *Nature*, 585, 357, doi: [10.1038/s41586-020-2649-2](https://doi.org/10.1038/s41586-020-2649-2)
- Horne, K. 1986, *PASP*, 98, 609, doi: [10.1086/131801](https://doi.org/10.1086/131801)
- Hu, R., Ehlmann, B. L., & Seager, S. 2012, *ApJ*, 752, 7, doi: [10.1088/0004-637X/752/1/7](https://doi.org/10.1088/0004-637X/752/1/7)
- Hunter, J. D. 2007, *Computing in Science & Engineering*, 9, 90, doi: [10.1109/MCSE.2007.55](https://doi.org/10.1109/MCSE.2007.55)
- Ih, J., Kempton, E. M. R., Whittaker, E. A., & Lessard, M. 2023, *ApJL*, 952, L4, doi: [10.3847/2041-8213/ace03b](https://doi.org/10.3847/2041-8213/ace03b)
- Iyer, A. R., Line, M. R., Muirhead, P. S., Fortney, J. J., & Gharib-Nezhad, E. 2023, *ApJ*, 944, 41, doi: [10.3847/1538-4357/acabc2](https://doi.org/10.3847/1538-4357/acabc2)
- Johnstone, C. P. 2020, *ApJ*, 890, 79, doi: [10.3847/1538-4357/ab6224](https://doi.org/10.3847/1538-4357/ab6224)
- Kempton, E. M. R., Bean, J. L., Louie, D. R., et al. 2018, *PASP*, 130, 114401, doi: [10.1088/1538-3873/aadf6f](https://doi.org/10.1088/1538-3873/aadf6f)
- Kempton, E. M. R., Zhang, M., Bean, J. L., et al. 2023, *Nature*, 620, 67, doi: [10.1038/s41586-023-06159-5](https://doi.org/10.1038/s41586-023-06159-5)
- Kendrew, S., Scheithauer, S., Bouchet, P., et al. 2015, *PASP*, 127, 623, doi: [10.1086/682255](https://doi.org/10.1086/682255)
- Kite, E. S., & Barnett, M. N. 2020, *Proceedings of the National Academy of Science*, 117, 18264, doi: [10.1073/pnas.2006177117](https://doi.org/10.1073/pnas.2006177117)
- Koll, D. D. B., Malik, M., Mansfield, M., et al. 2019, *ApJ*, 886, 140, doi: [10.3847/1538-4357/ab4c91](https://doi.org/10.3847/1538-4357/ab4c91)
- Kreidberg, L. 2015, *PASP*, 127, 1161, doi: [10.1086/683602](https://doi.org/10.1086/683602)
- Kreidberg, L., Koll, D. D. B., Morley, C., et al. 2019, *Nature*, 573, 87, doi: [10.1038/s41586-019-1497-4](https://doi.org/10.1038/s41586-019-1497-4)
- Lucy, L. B., & Sweeney, M. A. 1971, *AJ*, 76, 544, doi: [10.1086/111159](https://doi.org/10.1086/111159)
- Mahajan, A. S., Eastman, J. D., & Kirk, J. 2024, *ApJL*, 963, L37, doi: [10.3847/2041-8213/ad29f3](https://doi.org/10.3847/2041-8213/ad29f3)
- Malik, M., Kempton, E. M. R., Koll, D. D. B., et al. 2019a, *ApJ*, 886, 142, doi: [10.3847/1538-4357/ab4a05](https://doi.org/10.3847/1538-4357/ab4a05)
- Malik, M., Kitzmann, D., Mendonça, J. M., et al. 2019b, *AJ*, 157, 170, doi: [10.3847/1538-3881/ab1084](https://doi.org/10.3847/1538-3881/ab1084)
- Malik, M., Grosheintz, L., Mendonça, J. M., et al. 2017, *AJ*, 153, 56, doi: [10.3847/1538-3881/153/2/56](https://doi.org/10.3847/1538-3881/153/2/56)
- Mann, A. W., Dupuy, T., Kraus, A. L., et al. 2019, *ApJ*, 871, 63, doi: [10.3847/1538-4357/aaf3bc](https://doi.org/10.3847/1538-4357/aaf3bc)
- Mansfield, M., Kite, E. S., Hu, R., et al. 2019, *ApJ*, 886, 141, doi: [10.3847/1538-4357/ab4c90](https://doi.org/10.3847/1538-4357/ab4c90)
- Moran, S. E., Stevenson, K. B., Sing, D. K., et al. 2023, *ApJL*, 948, L11, doi: [10.3847/2041-8213/accb9c](https://doi.org/10.3847/2041-8213/accb9c)
- Nakayama, A., Ikoma, M., & Terada, N. 2022, *ApJ*, 937, 72, doi: [10.3847/1538-4357/ac86ca](https://doi.org/10.3847/1538-4357/ac86ca)
- Rackham, B. V., Apai, D., & Giampapa, M. S. 2018, *ApJ*, 853, 122, doi: [10.3847/1538-4357/aaa08c](https://doi.org/10.3847/1538-4357/aaa08c)
- Redfield, S., Batalha, N., Benneke, B., et al. 2024, arXiv e-prints, arXiv:2404.02932, doi: [10.48550/arXiv.2404.02932](https://doi.org/10.48550/arXiv.2404.02932)
- Spencer, J. R. 1990, *Icarus*, 83, 27, doi: [10.1016/0019-1035\(90\)90004-S](https://doi.org/10.1016/0019-1035(90)90004-S)
- STScI Development Team. 2013, pysynphot: Synthetic photometry software package, Astrophysics Source Code Library, record ascl:1303.023
- Tian, F. 2009, *ApJ*, 703, 905, doi: [10.1088/0004-637X/703/1/905](https://doi.org/10.1088/0004-637X/703/1/905)
- Trifonov, T., Caballero, J. A., Morales, J. C., et al. 2021, *Science*, 371, 1038, doi: [10.1126/science.abd7645](https://doi.org/10.1126/science.abd7645)
- Virtanen, P., Gommers, R., Burovski, E., et al. 2021, *scipy/scipy: SciPy 1.6.3, v1.6.3, Zenodo, Zenodo*, doi: [10.5281/zenodo.4718897](https://doi.org/10.5281/zenodo.4718897)
- Weiner Mansfield, M., Xue, Q., Zhang, M., & Koll, D. 2024, Data Behind the Figures: No Thick Atmosphere on the Terrestrial Exoplanet Gl 486b, 1.0, Zenodo, doi: [10.5281/zenodo.13774461](https://doi.org/10.5281/zenodo.13774461)
- West, A. A., Hawley, S. L., Bochanski, J. J., et al. 2008, *AJ*, 135, 785, doi: [10.1088/0004-6256/135/3/785](https://doi.org/10.1088/0004-6256/135/3/785)
- Whittaker, E. A., Malik, M., Ih, J., et al. 2022, *AJ*, 164, 258, doi: [10.3847/1538-3881/ac9ab3](https://doi.org/10.3847/1538-3881/ac9ab3)
- Xue, Q., Bean, J. L., Zhang, M., et al. 2024, arXiv e-prints, arXiv:2408.13340. <https://arxiv.org/abs/2408.13340>
- Zahnle, K. J., & Catling, D. C. 2017, *ApJ*, 843, 122, doi: [10.3847/1538-4357/aa7846](https://doi.org/10.3847/1538-4357/aa7846)
- Zhang, M., Hu, R., Inglis, J., et al. 2024, *ApJL*, 961, L44, doi: [10.3847/2041-8213/ad1a07](https://doi.org/10.3847/2041-8213/ad1a07)
- Zieba, S., Kreidberg, L., Ducrot, E., et al. 2023, *Nature*, 620, 746, doi: [10.1038/s41586-023-06232-z](https://doi.org/10.1038/s41586-023-06232-z)